Supporting Information

Breuer et al. 10.1073/pnas.1316156111

SI Text

Calculation of Electronic Coupling Matrix Elements. ***Derivation of correction factor*** c_{corr}. In the standard fragment-orbital density functional theory (FODFT) method for calculation of H_{ab}, the diabatic states are constructed by combining Kohn–Sham orbitals optimized for the two isolated monomer fragments in the gas phase (1, 2). Thus, spurious delocalization of the excess electron hole due to the electron delocalization error of standard exchange correlation functionals is avoided, but possible electronic polarization effects between the two monomers are missing. To estimate this contribution, coupling matrix elements obtained with FODFT were compared with values obtained with constrained density functional theory (CDFT) (3) as implemented in CPMD (1), where the diabatic states are constructed by optimizing the density for the dimer in the gas phase subject to a constraint on the charge difference between donor and acceptor.

We found that CDFT(PBE) optimizations (i.e., using the Perdew–Burke–Ernzerhof, or PBE, density functional) on the heme dimers taken from the protein structure resulted in relatively large spin leakage from the ferric to the ferrous heme. Although we have not investigated this problem further, it is likely that it can be cured by using CDFT with exact exchange functionals (4). Instead, we found that CDFT(PBE) calculations on a set of idealized dimer structures as used by Smith et al. (5) were straightforward and did not yield spurious spin delocalization. Hence, we used the five heme dimer structures of Smith et al. (5) at an Fe-Fe distance of 16.0 Å for the comparison between CDFT and FODFT calculations (Table S3). All calculations used the same electronic structure method as for the calculations on the heme pairs in the protein, i.e., PBE functional, a 130 Ryd plane wave cutoff, and Goedecker–Teter–Hutter pseudopotentials (semicore for Fe). We found that for each configuration, the ratio H_{ab}(CDFT)/H_{ab}(FODFT) lies close to their average of 1.75. The latter can be regarded as a correction factor for the missing electronic polarization between donor and acceptor in the FODFT calculations.

In the FODFT quantum mechanics/molecular mechanics (QM/MM) method, the calculation of H_{ab} is carried out similarly as above for the gas phase. The only difference is that the density of one monomer fragment is optimized in the static electrostatic field created by the force field charges of the other monomer fragment, the protein, and the solvent (the MM part). As mentioned in the main text, the effect of the MM part on the coupling values is negligibly small, not more than about 10%. This small effect probably means that the electronic polarization between donor and acceptor is not effectively mimicked by the charges of the MM fragment (a compensation between the latter and the protein/water seems unlikely). Thus, to account for the missing electronic polarization effects between the two fragments, we opted to apply the same correction factor as obtained from the gas-phase calculations above, i.e., the H_{ab}(FODFT) values obtained from QM/MM are multiplied by $c_{corr} = \langle H_{ab}(\text{CDFT})/H_{ab}(\text{FODFT})\rangle = 1.75$ as indicated in Eq. **2**. Table S1 summarizes the corrected FODFT QM/MM H_{ab} values for the heme pairs in the crystal structure and averaged over molecular dynamics (MD) trajectories. The latter were used for the calculation of electron transfer (ET) rates.

Impact of functional on FODFT couplings. To check whether the particular choice of the generalized gradient approximation functional had any impact on the coupling matrix elements, we also calculated FODFT couplings for the five test dimers above using the BLYP functional (i.e., Becke exchange part, Lee–Yang–Parr correlation part) instead of PBE. The numbers obtained were virtually identical. To check whether exact exchange was relevant to FODFT couplings between the protein cofactors, PBE and PBE0 were compared for the nine heme pairs in the crystal structure of MtrF (at a lower plane wave cutoff of 90 Ryd to keep the exact exchange calculations feasible and in the gas phase). As shown in Table S4, for the majority of pairs, the difference between PBE and PBE0 is relatively small. The average change from PBE to PBE0 is around 10%; although individual changes are larger, if they average out to a small global change here then something similar could be expected for the ensemble averages to be calculated from the snapshots extracted from MD. It was hence concluded that exact exchange effects could be neglected in calculating the FODFT ensemble averages $\langle |H_{ab}|^2 \rangle$.

Electronic Coupling Decay: Edge-to-Edge vs. Fe-Fe Distance Metric. In addition to the edge-to-edge distance metric used in Fig. 2, we also determined the coupling decay with respect to the Fe-Fe distance (Fig. S2). For the T-shaped and coplanar pairs, this yields a decay constant $\beta = 0.6$ Å^{-1} ($R^2 = 0.79$), similar to the 0.8 Å^{-1} ($R^2 = 0.85$) for edge-to-edge distance owing to the fact that both distances increase in the same way (the Fe-Fe distance increases by about 1 Å for every 1-Å increase in the edge-to-edge distance). For the stacked pairs, however, the Fe-Fe distance yields a lower decay constant: $\beta = 1.05$ Å^{-1} ($R^2 = 0.96$) compared with 2.25 Å^{-1} ($R^2 = 0.9997$) for edge-to-edge distance. This decrease in β can be rationalized by the fact that for the stacked pairs, the Fe-Fe distance increases about twice as fast as the edge-to-edge distance (i.e., for an edge-to-edge distance increase of 1 Å the Fe-Fe distance increases by around 2 Å) so that the distance decay is just about half as strong. A global fit would yield a decay constant of $\beta = 1.30$ Å^{-1} ($R^2 = 0.90$) compared with $\beta = 1.65$ Å^{-1} ($R^2 = 0.91$) for edge-to-edge, but the two individual fits describe the individual bin points better as measured by average absolute differences between bin points and regression. Thus, the two metrics give a similar description for coplanar and the T-shaped motifs, but the edge-to-edge distance metric is clearly superior for stacked pairs (R^2 very close to 1). The latter metric's better performance stems from the fact that, according to DFT calculations, the atoms of the macrocycles contribute to the electron mediating molecular orbitals with their p_z atomic orbitals (Fig. 1*C*) and one can expect that the overlap between these p_z atomic orbitals determines to a large extent the total electronic coupling.

Analytical Model Describing Electron Flux Through MtrF. We derive an analytical function for the electron flux J as a function of k_{out} (Fig. 4) by coarse graining the states of the system. We assume that electron transport in MtrF can be modeled by four distinct sites A to D: site A corresponds to an external donor injecting electrons into the protein; site B denotes the protein electron entrance site; site C represents the protein electron egress site; and site D denotes an external electron acceptor. The kinetics is then described by the following scheme:

$$\mathrm{A} \xrightarrow{k_{in}} \mathrm{B} \underset{k_b}{\overset{k_f}{\rightleftharpoons}} \mathrm{C} \xrightarrow{k_{out}} \mathrm{D}, \qquad \textbf{[S1]}$$

where electron injection into the protein (A to B) and ejection from the protein (C to D) is considered irreversible as can be assumed to be the case in the experiments of White et al. (6). The complicated kinetics of electron flux through the protein is condensed into one effective forward and backward rate constant k_f

and k_b, respectively. Under steady-state conditions, the net flux J between any two adjacent sites is equal

$$J = k_{in}(1-P_B) = k_f P_B(1-P_C) - k_b(1-P_B)P_C = k_{out}P_C, \quad \textbf{[S2]}$$

where P_B and P_C denote populations in the interval [0, 1]. The populations of A and D are assumed to be 1 and 0 at all times, i.e., the electron donor is in excess concentrations and the electron on the acceptor is immediately removed from equilibrium. Hence these populations do not appear in the expression for the flux. The factors $(1 - P_B)$ and $(1 - P_C)$ account for the fact that sites B and C can only be occupied by at most one single electron. We thus have two equations for the two unknowns P_B and P_C. Solving for P_B in terms of P_C and reinserting to solve for P_C yields the equation

$$P_C = \left(\frac{k_f}{k_{in}} - \frac{k_b}{k_{in}}\right)P_C^2 - \left(\frac{k_f}{k_{in}} + \frac{k_f}{k_{out}}\right)P_C + \frac{k_f}{k_{out}}. \quad \textbf{[S3]}$$

In the limit of high electron injection rates, $k_{in} \gg k_f, k_b$, Eq. **S3** reduces to the simple expression

$$P_C = \frac{k_f}{k_f + k_{out}}. \quad \textbf{[S4]}$$

Insertion of Eq. **S4** in the last identity of Eq. **S2** gives

$$J = \frac{k_f}{1 + \frac{k_f}{k_{out}}}. \quad \textbf{[S5]}$$

Thus, for high injection rates, the flux through the protein depends only on the effective forward rate k_f and the ejection rate k_{out}. Furthermore, if we take the limit $k_{out} \to \infty$, J becomes equal to k_f. The latter in fact represents the maximal possible flux J_{max} through the protein. We can therefore rewrite Eq. **S5** as

$$J = \frac{J_{max}}{1 + \frac{J_{max}}{k_{out}}}. \quad \textbf{[S6]}$$

Fig. S3 shows the curves for J vs. k_{out} along the octa-heme chain of MtrF in the 10 → 5 and 5 → 10 direction as obtained by solving the master equation for the full problem (solid lines). Fits to Eq. **S6** (dash-dotted lines) match the respective data very well, with values $J_{max} = 1.57 \times 10^4$ for the forward and $J_{max} = 1.06 \times 10^4$ for the backward direction. Thus, the full kinetic problem can be successfully mapped on the coarse four-state model in Eq. **S1**.

Modeling of Electron Flux Through MtrCAB. In the following, we try to model electron flux through the multiheme protein complex MtrCAB, i.e., the transmembrane complex assembled in a proteoliposome by White et al. (6), where electrons are transported from liposome-contained methyl viologen via MtrCAB to external iron oxides. MtrA is known to be a deca-heme cytochrome (7), whereas MtrB is a membrane pore protein proposed to enable close contact between MtrA and MtrC (8). We thus need a model and ET parameters for MtrC, MtrA, and the contact between them. For MtrC, we use our ET parameters for MtrF motivated by the homology model of ref. 9, and we assume electron transport along the octa-heme chain from heme 10 to heme 5 (egress site). The structure of MtrA is not known; however, the heme-binding motifs in its N-terminal half can be sequence-aligned with the penta-heme cytochrome NrfB (10), and MtrA has been found to be of a rod-like shape of around 100 Å length (11). We therefore decided to model MtrA as a NrfB head-to-tail homodimer. We can then use our regressions for the two coupling regimes in Fig. 2 to estimate approximate couplings for the heme pairs in the crystal structure of NrfB (12), as well as for the contact between the two NrfB subunits on the one hand and between NrfB and MtrC/F on the other hand (by some crude manual docking of protein structures that should suffice for this modeling). In regard to reorganization free energies, the most significant difference should occur between heme pairs located in the solvent-exposed part of MtrA and those located within the membrane-buried part making contact to MtrC. With a membrane thickness of around 40–50 Å (6), MtrA should be roughly half-buried into the membrane, with the other half exposed into the periplasm. Thus, for the first five heme pairs (as well as the final MtrA-MtrC contact), we assume a reorganization free energy λ of 0.9 eV (i.e., a typical number for MtrF), whereas for the four remaining membrane-buried pairs, we assume 0.57 eV, the reorganization energy previously obtained (13) for heme *a* to heme a_3 ET in membrane-embedded cytochrome *c* oxidase. The final set of parameters to be estimated are then the driving forces of each ET step. Although the overall electrochemical response of MtrA has been studied (8), redox potentials of individual cofactors are not known. A crude fit to the voltammogram in Hartshorne et al. (8) yields a set of 10 distinct redox potentials, however, that enable to estimate minimal and maximal flux through MtrCAB within the model described thus far, by assigning redox potentials to the 10 cofactors of MtrA to either yield the smallest possible or highest possible rate-limiting single ET rate. We thereby obtain the two curves in Fig. S4, delimiting upper and lower limits for the flux through MtrCAB based on our model. As can be seen, depending on the combination of parameters the flux through MtrCAB could reach the same level as for MtrF itself (maximal flux for flux-maximizing parameters, black curve: 14,300 s^{-1}); it could also be one order of magnitude smaller than for MtrF (maximal flux for flux-minimizing parameters, blue curve: 800 s^{-1}), but this is rather unlikely as it requires the steepest possible free energy uphill step to have a small electronic coupling and a high reorganization energy.

Current-Voltage Response of MtrF in Solution and in Air. ***Modeling of current-voltage response.*** Pioneering measurements using an atomic force microscopy tip and a gold electrode revealed that bacterial pili can support very high currents of several nano-Ampere at moderate voltages (14, 15). It is generally thought that the conduction along pili is facilitated by multiheme proteins, and that when a multiheme protein is sandwiched between two electrodes, the conduction occurs via electron hopping along the heme groups (16, 17). Here we would like to investigate if the hopping mechanism can account for the observed nano-Ampere currents when the ET parameters are used that are reported in our current and previous works. To this end, we model the current-voltage response of a single MtrF protein placed between two electrodes with potential difference V by solving a master equation similarly as described in the main text (see below for details), but with the vital difference that the driving force for heme-heme ET is gradually decreased by $eV/(n + 1)$ as the electrode potential difference is stepped up (e is the unit charge and n the number of hemes between the left and the right electrodes).

The current-voltage characteristic obtained for the calculated ET parameters in solution is illustrated in Fig. S5 (black lines). Two different regimes are shown depending on the ratio of heterogeneous input (=output) rate, $k_{10,in}(=k_{5,out})$ and the smallest heme-heme ET rate, k_{ji}^{min} evaluated at zero potential bias, $r = k_{10,in}/k_{ji}^{min}$. The current shown in solid lines ($r = 100$) is limited by ET through MtrF, and the current shown in dash dotted lines ($r = 1$) is, where different from the solid line, limited by heterogenous ET. We find that the increase in current is approximately linear at low voltages but sharply increases to a maximum at $V \approx (n+1)\lambda/e$ to decrease for higher voltages. The

existence of a maximum is a consequence of the parabolic relationship between $\log k_{ET}$ and ΔA (Eq. **3**). The maximum current we obtain at protein-limiting conditions is 36 picoampere (pA) at a voltage of 8.2 V.

Previous experimental *I-V* measurements on conductive pili were carried out in air rather than solution. To account for the different environmental conditions, we reduce all reorganization free energies by around 50% (18–20) and set the heme redox potential differences, i.e., driving forces, all equal to zero (see details below for a justification). The resultant *I-V* curves are shown in red for $r = 10$ (solid line) and $r = 1$ (dash dotted). We observe again a linear increase in the current for low voltages (see inset), but a significant shift of the position of the maximum to smaller voltages, as is expected from the above relation between λ and *V*. The maximum current at protein-limiting conditions is 58 pA at 3.6 V. Thus, our calculations suggest that the surrounding medium (air/solution) has a large effect on the voltage range but only a relatively small effect on the maximum current.

Discussion. Although our calculations are consistent with the kinetic measurements of White et al. (6) on MtrCAB, they do not reproduce the nano-Ampere currents observed in current-voltage measurements on bacterial pili (14, 15). Two factors could contribute to this discrepancy. (*i*) The measurements were directly conducted on the pili, and it is unknown how many proteins mediate the current. In ref. 16, it was estimated that the single protein current should be multiplied by at most a factor of 10^3, which would indeed shift the calculated pA currents into the nano-Ampere regime. However, we believe that a more realistic upper estimate would be one to two orders of magnitude lower as the factor of 10^3 was based on a hypothetical closest packing of hemes without any protein matrix. Hence, it is unlikely that the discrepancy can be explained by the protein number density alone. (*ii*) We assumed that the current in MtrF is mediated by electron hopping between neighboring $Fe^{2+/3+}$-hemes according to Eq. **1**. Although this is almost certainly the dominating ET mechanism in the kinetic experiments on MtrCAB (6), it may not be the dominating conduction channel in the *I-V* measurements. A possible alternative could be that conduction is predominantly mediated by higher-lying, nonoccupied electronic states (21), such as the e_g manifold of the low-spin hemes or more delocalized states of the porphyrine ring. In this case, all hemes are likely to be in their reduced (neutral) state and temporarily adopt a negative charge when the conducting electron passes by.

Modeling details. The curves in Fig. S5 are calculated using the convention $I = -J$. For calculation of the heme-to-heme ET rates in solution, the same H_{ab} and λ values are used as in the main text (summarized in Table S1), but with suitably modified driving forces: $\Delta A \to \Delta A - eV/(n+1)$. The heterogeneous ET steps between heme 10 and the left electrode and heme 5 and the right electrode are treated as reversible (i.e., $k_{10,out}, k_{5,in} \neq 0$) and symmetric (i.e., $k_{10,in} = k_{5,out}$ and $k_{10,out} = k_{5,in}$) and are obtained via the electrochemical form of the nonadiabatic ET rate equation (16, 22)

$$k_{10,in} = C_{elec} \int_{-\infty}^{+\infty} \frac{\exp\left[-\left(x - \frac{\lambda + e(E - E_{10})}{k_B T}\right)^2 \left(\frac{k_B T}{4\lambda}\right)\right]}{1 + \exp(x)} dx, \quad \textbf{[S7]}$$

$$k_{10,out} = C_{elec} \int_{-\infty}^{+\infty} \frac{\exp\left[-\left(x - \frac{\lambda - e(E - E_{10})}{k_B T}\right)^2 \left(\frac{k_B T}{4\lambda}\right)\right]}{1 + \exp(x)} dx, \quad \textbf{[S8]}$$

where λ is the reorganization energy of the heterogeneous ET step, *E* is the potential level at the electrode, E_{10} is the potential at heme 10, C_{elec} is a constant denoting the average coupling between heme and electrode, and k_B and *T* are Boltzmann constant and temperature, respectively. Hence, to estimate the heterogeneous ET rates at the electrodes via this pair of equations, estimates are needed for the reorganization free energy λ, the local potential drop $E - E_{10}$, and the coupling constant C_{elec}. Although no values are available for the reorganization free energy of MtrF in contact with an electrode, electrochemical measurements of WT and mutated cytochrome *c* on a gold electrode (23) yielded reorganization free energies of around 0.45 eV, which we chose to use in our model of current-voltage response in solution. For the potential drop at the electrode, we made the assumption that it is comparable to the voltage drop between adjacent hemes, which we also assumed to be equal (ignoring minor differences due to the nonlinear arrangement of hemes along the octa-heme chain): i.e., all potential drops were set to $V/(n + 1)$ with *n* as the number of redox sites between the two electrodes (eight for electron transport along the octa-heme chain), i.e., $1/(n + 1) = 0.11$, which is similar to experimental estimates (14). For the electrode contacts, $1/2 \times \Delta E^0_{10\to5}$, half the redox potential difference between the terminal hemes 10 and 5 was added to correct for the unequal potential levels of the terminal hemes at zero bias potential (yielding a nonzero current at zero potential otherwise).

The remaining parameter is then C_{elec}, the constant summarizing the overall coupling between terminal redox site and electrode. Rather than just making one assumption for this electrode-protein coupling, we tried different values to obtain the current-voltage response in different regimes. For $r = 100$ (solution) and $r = 10$ (air), respectively (see above for the definition of *r*), we observe that the heterogeneous transfer rate at the electrodes is larger than the smallest intraprotein rate, indicating that for this value (and higher values) of *r* the current-voltage response is protein limited, giving rise to a clear maximum in *I* in Fig. S5 (solid lines), indicating the transition between normal and inverted Marcus regime for nonadiabatic ET. Decreasing *r* to 1 yields the broken lines that for dry conditions at first show an electrode-limited response, reaching a constant current indicating the maximal overlap between Gaussian redox peak and Fermi distribution in Eq. **S7**, until the slowest protein rate becomes slower than the heterogeneous rate on which the curve matches the corresponding curve for higher *r* again. For solution conditions, only the electrode-limited regime is visible in the potential range studied.

Under dry conditions, i.e., for a measurement in ambient air, we assume the couplings to stay the same given that these depend only on the heme cofactor arrangement that should not change significantly. In regard to the reorganization free energies, a significant change can be expected given that they are known to be highly affected by the solvent environment. Specifically, Tipmanee et al. (20) found for a set of model ET proteins that the solvent contributed one-half to three-quarters of the total reorganization free energy. Without more precise information on the corresponding solvent contributions in MtrF, we chose a λ of 0.4 eV for intraprotein ET and 0.2 eV at the protein-electrode interface for our ambient air model. In regard to driving forces, no information is available on these under dry conditions, but it can be assumed that without a solvation shell, ionizable groups should be either unionized or binding a counter ion so that the electrostatic potential in ambient air should be much more homogeneous than in water. We therefore decided to set all intrinsic driving forces equal to zero so that the total driving forces are equal to the contribution from the external potential. Obviously this crude set of parameters does not allow for detailed predictions and is only used to get an idea what the current-voltage behavior might be under dry conditions.

1. Oberhofer H, Blumberger J (2010) Electronic coupling matrix elements from charge constrained density functional theory calculations using a plane wave basis set. *J Chem Phys* 133(24):244105.
2. Oberhofer H, Blumberger J (2012) Revisiting electronic couplings and incoherent hopping models for electron transport in crystalline C60 at ambient temperatures. *Phys Chem Chem Phys* 14(40):13846–13852.
3. Wu Q, Van Voorhis T (2005) Direct optimization method to study constrained systems within density-functional theory. *Phys Rev A* 72(2):024502-1–024502-4.
4. Blumberger J, McKenna KP (2013) Constrained density functional theory applied to electron tunnelling between defects in MgO. *Phys Chem Chem Phys* 15(6):2184–2196.
5. Smith DMA, Rosso KM, Dupuis M, Valiev M, Straatsma TP (2006) Electronic coupling between heme electron-transfer centers and its decay with distance depends strongly on relative orientation. *J Phys Chem B* 110(31):15582–15588.
6. White GF, et al. (2013) Rapid electron exchange between surface-exposed bacterial cytochromes and Fe(III) minerals. *Proc Natl Acad Sci USA* 110(16):6346–6351.
7. Pitts KE, et al. (2003) Characterization of the Shewanella oneidensis MR-1 decaheme cytochrome MtrA: Expression in Escherichia coli confers the ability to reduce soluble Fe(III) chelates. *J Biol Chem* 278(30):27758–27765.
8. Hartshorne RS, et al. (2009) Characterization of an electron conduit between bacteria and the extracellular environment. *Proc Natl Acad Sci USA* 106(52):22169–22174.
9. Edwards MJ, Fredrickson JK, Zachara JM, Richardson DJ, Clarke TA (2012) Analysis of structural MtrC models based on homology with the crystal structure of MtrF. *Biochem Soc Trans* 40(6):1181–1185.
10. Clarke TA, et al. (2008) The role of multihaem cytochromes in the respiration of nitrite in Escherichia coli and Fe(III) in Shewanella oneidensis. *Biochem Soc Trans* 36(Pt 5): 1005–1010.
11. Firer-Sherwood MA, Ando N, Drennan CL, Elliott SJ (2011) Solution-based structural analysis of the decaheme cytochrome, MtrA, by small-angle X-ray scattering and analytical ultracentrifugation. *J Phys Chem B* 115(38):11208–11214.
12. Clarke TA, Cole JA, Richardson DJ, Hemmings AM (2007) The crystal structure of the pentahaem c-type cytochrome NrfB and characterization of its solution-state interaction with the pentahaem nitrite reductase NrfA. *Biochem J* 406(1):19–30.
13. Tipmanee V, Blumberger J (2012) Kinetics of the terminal electron transfer step in cytochrome c oxidase. *J Phys Chem B* 116(6):1876–1883.
14. El-Naggar MY, et al. (2010) Electrical transport along bacterial nanowires from Shewanella oneidensis MR-1. *Proc Natl Acad Sci USA* 107(42):18127–18131.
15. Gorby YA, et al. (2006) Electrically conductive bacterial nanowires produced by Shewanella oneidensis strain MR-1 and other microorganisms. *Proc Natl Acad Sci USA* 103(30):11358–11363.
16. Polizzi NF, Skourtis SS, Beratan DN (2012) Physical constraints on charge transport through bacterial nanowires. *Faraday Discuss* 155:43–62, discussion 103–114.
17. Pirbadian S, El-Naggar MY (2012) Multistep hopping and extracellular charge transfer in microbial redox chains. *Phys Chem Chem Phys* 14(40):13802–13808.
18. Blumberger J, Klein ML (2006) Reorganization free energies for long-range electron transfer in a porphyrin-binding four-helix bundle protein. *J Am Chem Soc* 128(42): 13854–13867.
19. Blumberger J (2008) Free energies for biological electron transfer from QM/MM calculation: Method, application and critical assessment. *Phys Chem Chem Phys* 10(37):5651–5667.
20. Tipmanee V, Oberhofer H, Park M, Kim KS, Blumberger J (2010) Prediction of reorganization free energies for biological electron transfer: A comparative study of Ru-modified cytochromes and a 4-helix bundle protein. *J Am Chem Soc* 132(47):17032–17040.
21. Migliore A, Nitzan A (2013) Irreversibility and hysteresis in redox molecular conduction junctions. *J Am Chem Soc* 135(25):9420–9432.
22. Chidsey CED (1991) Free energy and temperature dependence of electron transfer at the metal-electrolyte interface. *Science* 251(4996):919–922.
23. Bortolotti CA, et al. (2011) The reorganization energy in cytochrome c is controlled by the accessibility of the heme to the solvent. *J Phys Chem Lett* 2(14):1761–1765.

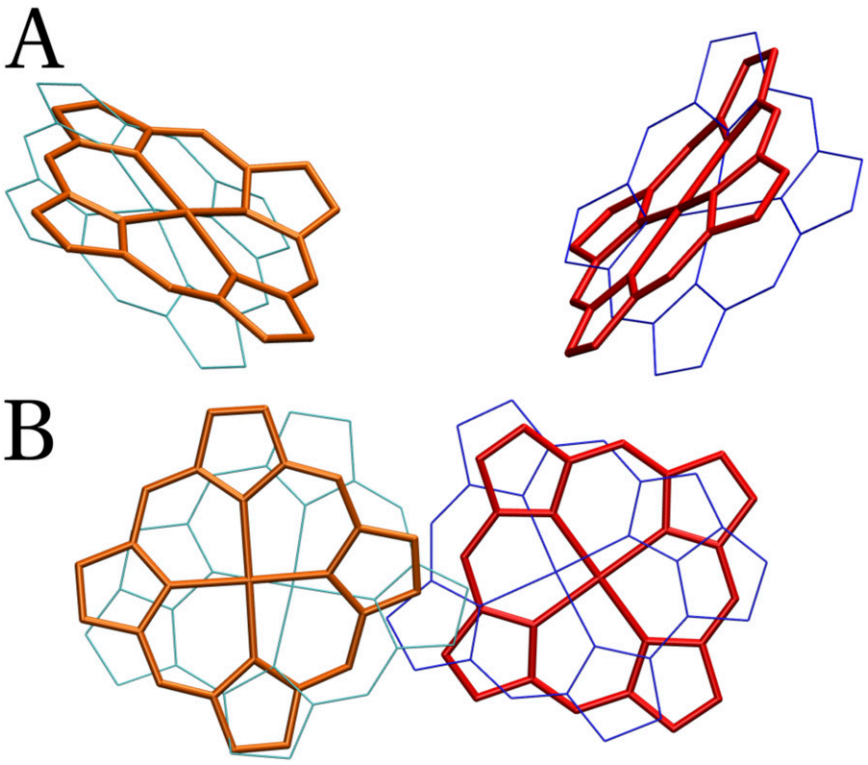

Fig. S1. Comparison of heme dimer motifs in MtrF with metal-containing porphyrin dimers in other ET-related proteins. (*A*) T-shaped pair 6–8 from MtrF (red/orange) vs. heme a-heme a_3 from cytochrome *c* oxidase [blue/cyan; Protein Databank (PDB) ID 1V54]. (*B*) Stacked pair 4–5 from MtrF (red/orange) vs. the chlorophyll-special pair from the photosynthetic reaction center from *Rh. sphaeroides* (blue/cyan; PDB ID 1M3X).

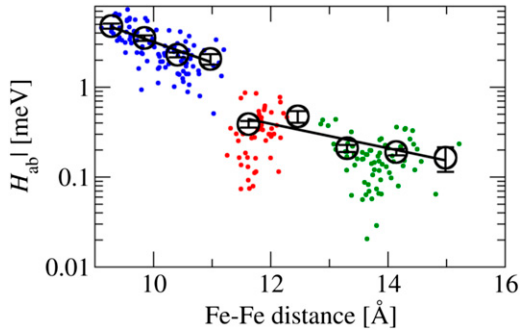

Fig. S2. Modulus of electronic coupling matrix elements ($|H_{ab}|$) for ET between ferrous and ferric heme cofactors in MtrF as a function of the heme Fe-Fe distance. Data points and fits are obtained as explained in Fig. 2, and the same color code is used. Bin width for $\langle |H_{ab}|^2 \rangle^{\frac{1}{2}}$ (circles) is 0.5625 (*Left*) and 0.7 Å (*Right*).

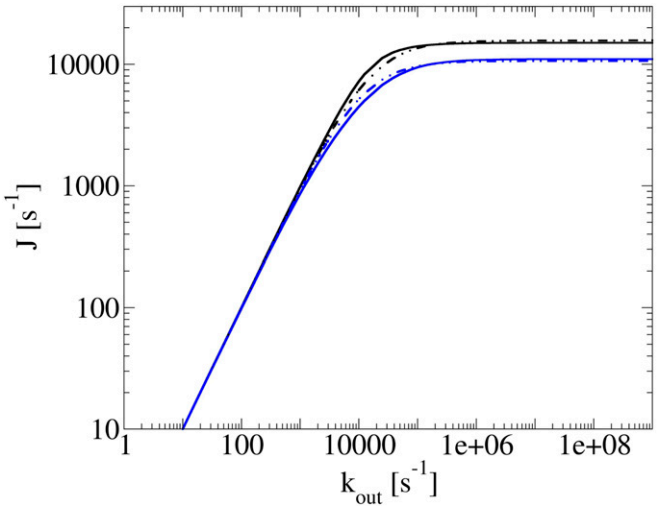

Fig. S3. J vs. k_{out} for electron flux along the octa-heme chain in MtrF in both directions (solid lines; black: forward/10 → 5, blue: backward/5 → 10), together with analytic fits to the numeric curves using Eq. **S6** (broken lines).

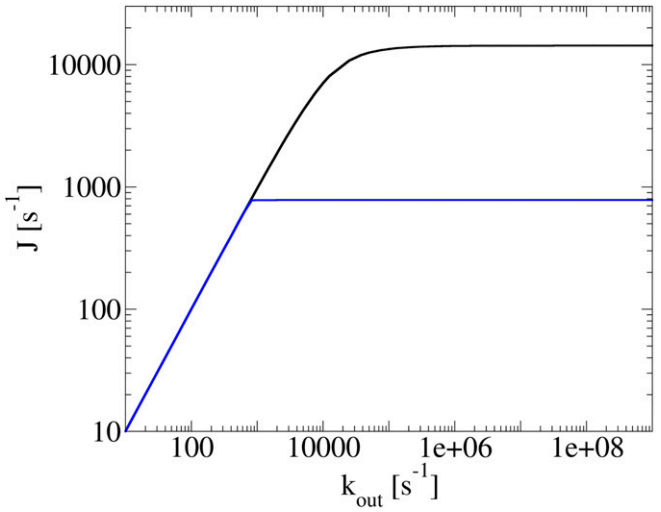

Fig. S4. J vs. k_{out} for electron flux through the protein complex MtrCAB (see text for model applied). Black curve: redox potentials in MtrA chosen to maximize flux; blue curve: redox potentials chosen to minimize flux.

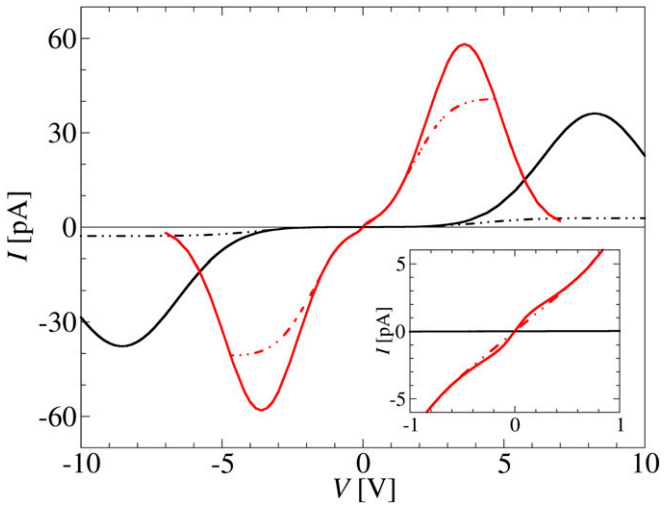

Fig. S5. Current (*I*)-voltage (*V*) response of a single MtrF molecule in solution (black lines) and in air (red lines) assuming electron hopping as the conduction channel. Two different regimes are shown, protein limiting [$r = 100$ (black solid line), $r = 10$ (red solid line)] and electrode-protein limiting [$r = 1$ (black and red dash dotted lines)]. See text for definition of r.

Table S1. Coupling matrix elements $|H_{ab}|$ obtained from QM/MM FODFT calculations according to Eq. 2 ($c_{corr} = 1.75$), driving forces ΔA_{ji} (1), reorganization free energies λ (2), and heme-heme ET rates for solvated MtrF, k_{ji} and k_{ij}

Pair *i–j*	$\lvert H_{ab}\rvert$ (crystal structure) (meV)	$\langle\lvert H_{ab}\rvert^2\rangle^{\frac{1}{2}}$ (MD) (meV)	$\sigma(\lvert H_{ab}\rvert)$ (MD) (meV)	ΔA_{ji} (eV)	λ (eV)	k_{ji} (s^{-1})	k_{ij} (s^{-1})
1–2	0.27	0.24	0.09	0.02	1.13	1.18×10^{4}	2.19×10^{4}
1–3	0.31	0.49	0.21	0.12	0.96	2.89×10^{4}	3.37×10^{6}
1–6	0.08	0.13	0.05	0.01	0.94	2.68×10^{4}	3.95×10^{4}
3–4	1.71	2.21	0.67	0.10	0.75	8.10×10^{6}	4.19×10^{8}
4–5	2.34	3.63	1.26	−0.22	0.84	3.12×10^{9}	5.81×10^{5}
6–7	0.28	0.23	0.11	−0.13	1.06	2.99×10^{5}	2.38×10^{3}
6–8	0.29	0.31	0.16	0.10	0.87	4.47×10^{4}	2.31×10^{6}
8–9	2.64	2.31	1.08	0.13	0.93	8.46×10^{5}	1.11×10^{8}
9–10	4.59	4.52	1.52	−0.19	0.99	6.14×10^{8}	4.43×10^{5}

Electronic coupling for the single crystal structure configuration is compared with the root-mean-square average obtained from MD simulation, $\langle|H_{ab}|^2\rangle^{\frac{1}{2}}$, $\sigma = \langle(|H_{ab}| - \langle|H_{ab}|\rangle)^2\rangle^{\frac{1}{2}}$. The notation ΔA_{ji} and k_{ji} refers to ET from heme *i* to *j* and k_{ij} is for ET from heme *j* to *i*. Rate constants are calculated according to the nonadiabatic expression Eq. **3**. See Fig. 1 for definition of heme labels.

1. Breuer M, Zarzycki P, Blumberger J, Rosso KM (2012) Thermodynamics of electron flow in the bacterial deca-heme cytochrome MtrF. *J Am Chem Soc* 134(24):9868–9871.
2. Breuer M, et al. (2012) Molecular structure and free energy landscape for electron transport in the decahaem cytochrome MtrF. *Biochem Soc Trans* 40(6):1198–1203.

Table S2. Heme edge-to-edge distance *R* in the crystal structure of MtrF [PDB ID 3PMQ (1)] and the average and root-mean-square fluctuation obtained from 100-ns MD simulation

Pair	*R* (crystal structure) (Å)	⟨*R*⟩ (MD) (Å)	σ(*R*) (MD) (Å)
1–2	6.26	6.98	0.54
1–3	6.17	5.95	0.15
1–6	6.93	6.78	0.47
3–4	4.24	4.28	0.18
4–5	3.87	3.83	0.24
6–7	6.03	6.20	0.41
6–8	5.94	5.85	0.24
8–9	4.42	4.42	0.27
9–10	3.94	3.82	0.17

1. Clarke TA, et al. (2011) Structure of a bacterial cell surface decaheme electron conduit. *Proc Natl Acad Sci USA* 108(23):9384–9389.

Table S3. Coupling matrix elements $|H_{ab}|$ for five model heme dimers in the gas phase (1) as obtained with FODFT and CDFT

Structure	FODFT (meV)	CDFT (meV)	CDFT/FODFT
A	0.10	0.21	2.12
B	0.48	0.79	1.65
C	0.51	0.97	1.91
D	0.10	0.16	1.57
E	0.01	0.01	1.45

1. Smith DMA, Rosso KM, Dupuis M, Valiev M, Straatsma TP (2006) Electronic coupling between heme electron-transfer centers and its decay with distance depends strongly on relative orientation. *J Phys Chem B* 110(31):15582–15588.

Table S4. Coupling matrix elements $|H_{ab}|$ for the nine heme pairs in the crystal structure of MtrF [PDB ID 3PMQ (1)] as obtained from gas phase FODFT calculations according to Eq. 2 (c_{corr} = 1.75) using the PBE and PBE0 functional

Pair	PBE (meV)	PBE0 (meV)	PBE0/PBE
1–2	0.59	0.64	1.09
1–3	0.85	0.79	0.93
1–6	0.68	0.81	1.20
3–4	3.00	2.39	0.80
4–5	3.93	3.34	0.85
6–7	0.60	0.40	0.67
6–8	1.27	1.20	0.94
8–9	3.36	3.76	1.12
9–10	3.22	1.92	0.60

1. Clarke TA, et al. (2011) Structure of a bacterial cell surface decaheme electron conduit. *Proc Natl Acad Sci USA* 108(23):9384–9389.